

# A census of young stellar populations in the warm ULIRG PKS1345+12

J.Rodríguez Zaurín<sup>1</sup>\*, J.Holt<sup>1</sup>, C.N Tadhunter<sup>1</sup> and R.M.González Delgado<sup>2</sup>

<sup>1</sup>*Department of physics and Astronomy, University of Sheffield, Sheffield S3 7RH*

<sup>2</sup>*Instituto de Astrofísica de Andalucía(CSIC), P.O.Box 3004, 18080 Granada, Spain*

29 July 2018

## ABSTRACT

We present a detailed investigation of the young stellar populations (YSP) in the radio-loud ultra luminous infrared galaxy (ULIRG) PKS1345+12(z=0.12), based on high resolution *Hubble Space Telescope* (HST) imaging and long slit spectra taken with the *William Herschel Telescope* (WHT) on La Palma. While the images clearly show bright knots suggestive of super star clusters(SSC), the spectra reveal the presence of YSP in the diffuse light across the full extent of the halo of the merging-double nucleus system. Spectral synthesis modelling has been used to estimate the ages of the YSP for both the SSC and the diffuse light sampled by the spectra. For the SSC we find ages  $t_{SSC} < 6$  Myr with reddenings  $0.2 < E(B - V) < 0.5$  and masses  $10^6 < M_{SSC}^{YSP} < 10^7 M_{\odot}$ . In the region to the south of the western nucleus that contains the SSC our modelling of the spectrum of the diffuse light is also consistent with a relatively young age for the YSP ( $\sim 5$  Myr), although older YSP ages cannot be ruled out. However, in other regions of the galaxy we find that the spectra of the diffuse light component can only be modelled with a relatively old post-starburst YSP (0.04 – 1.0 Gyr) or with a disk galaxy template spectrum. The results demonstrate the importance of accounting for reddening in photometric studies of SSC, and highlight the dangers of focussing on the highest surface brightness regions when trying to obtain a general impression of the star formation activity in the host galaxies of ULIRGs. The case of PKS1345+12 provides clear evidence that the star formation histories of the YSP in ULIRGs are complex. While the SSC represent the vigorous phase of star formation associated with the final stages of the merger, the YSP in

the diffuse light are likely to represent star formation in one or more of the merging galaxies at an earlier stage or prior to the start of the merger.

Intriguingly, our long-slit spectra show line splitting at the locations of the SSC, indicating that they are moving at up to  $450 \text{ km s}^{-1}$  with respect to the local ambient gas. Given their kinematics, it is plausible that the SSC have been formed either in fast moving gas streams/tidal tails that are falling back into the nuclear regions as part of the merger process, or as a consequence of jet-induced star formation linked to the extended, diffuse radio emission detected in the halo of the galaxy.

**Key words:** Radio galaxies, ULIRGs, Young stellar populations, mergers, starbursts.

## 1 INTRODUCTION

A variety of surveys over the last two decades have revealed populations of galaxies that emit the bulk of their radiation at infrared wavelengths (Soifer & et al, 1984a,b; Houck & et al, 1984; Houck et al., 1985; Le Floc'h et al., 2005; Pérez-González et al., 2005). Such objects are thought to be responsible for most of the star formation activity in the distant Universe (Le Floc'h et al., 2005), while in the local Universe these galaxies are classified as Luminous ( $L_{ir} > 10^{11} \text{ L}_\odot$ ) or Ultraluminous ( $L_{ir} > 10^{12} \text{ L}_\odot$ ) infrared galaxies (LIRGs/ULIRGs). The morphologies of ULIRGs clearly suggest that most of them are recent or ongoing mergers. The presence of an AGN in a subset of these objects is also well known, with some ULIRGs classified as QSOs at optical wavelengths. For a more complete review of the properties of LIRGs/ULIRGs see Sanders & Mirabel (1996).

Much attention has been paid recently to the so-called warm ULIRGs (mid-infrared colours of  $f_{25}/f_{60} \geq 0.2$ )<sup>1</sup>. These objects represent the  $\sim 20\text{--}25\%$  of the total ULIRG population discovered by the IRAS satellite. Most of them have AGN optical spectra, very large molecular gas masses ( $M_{H_2} \sim 10^{10} \text{ M}_\odot$ : Sanders et al. 1988) and are found in an advanced merger state. In fact, Surace & Sanders (1999) found that 75% of the warm ULIRGs in their sample of 12 objects were associated with single nucleus galaxies. These properties suggest that such objects represent a transitional stage between cool ULIRGs and Radio Galaxies/QSOs (Sanders et al., 1988): cool ULIRGs evolve into warm ULIRGs on their way

\* E-mail: jrzaurin@sheffield.ac.uk

<sup>1</sup> The quantities  $f_{25}$  and  $f_{60}$  represent the *IRAS* flux densities (non-colour corrected) in units of Jy at 25 and 60  $\mu\text{m}$  respectively

to becoming QSOs/radio galaxies. Indeed, models predict that the tidal forces associated with mergers lead to large concentrations of gas and dust in the nuclear regions of the galaxies (Mihos & Hernquist, 1996; Barnes & Hernquist, 1996); such concentrations may trigger both AGN and starburst activity. However, the timing of the AGN relative to the major starburst triggered by the merger remains uncertain. Although some models assume that both starburst and AGN will occur simultaneously, when there is sufficient concentration of gas in the nuclear regions (di Matteo et al., 2005), the idea that cool ULIRGs evolve eventually into QSOs (Sanders et al., 1988) suggests that there may be a significant delay between the starburst and visible AGN activity.

Given that the models make specific predictions about the histories of the star formation triggered in the course of major gas-rich mergers, studies of the stellar populations in ULIRGs provide useful information about the mergers and, potentially, allow us to test the models. Moreover, for those ULIRGs with AGN and powerful radio jets, the ages of the young stellar populations (YSP) can be used to establish the order of events during the merger, for example, whether the AGN was activated before, at the same time as, or after the merger-induced starburst (Tadhunter et al., 2005; Emonts et al., 2006). Thus studies of the YSP have the potential to help us to understand the possible links between ULIRGs and AGN.

In this context, there have been surprisingly few studies of the YSP in ULIRGs. Two complementary approaches have been used in the past: one based on photometric analysis of images of the galaxies taken at different wavelengths, focused mainly on studying the YSP associated with the bright knots detected in the objects (Surace et al., 1998; Surace & Sanders, 1999; Surace & et al, 2000a,b; Wilson et al., 2006); the other comprising spectroscopic analysis of UV/optical spectra of more spatially extended regions (Canalizo & Stockton, 2000a,b, 2001; Tadhunter et al., 2005). Note that such optical studies sample the star formation in the systems prior to the current prodigious formation activity represented by the ULIRG that is likely to be hidden from view at optical wavelengths. In this paper we combine optical spectroscopy and imaging observation in order to investigate the YSP in the warm ULIRG/Radio Galaxy PKS1345+12

PKS1345+12 is a luminous, compact radio source (Evans et al., 1999; Holt et al., 2003) in an elliptical-like host galaxy (e.g. Axon et al. 2000). The galaxy has a clear double nucleus separated by  $\sim 1.8$  arcsec or  $4.3$  kpc<sup>2</sup>, and the AGN activity is associated with the western

<sup>2</sup>  $H_0 = 75$  km s<sup>-1</sup>,  $q_0 = 0.0$  assumed throughout resulting in a scale of  $2.37$  kpc arcsec<sup>-1</sup> at  $z = 0.122$

nucleus, which has a spectrum characteristic of narrow line radio galaxies (Evans et al., 1999; Holt et al., 2003).

Significant YSP have also been detected in PKS1345+12 at optical wavelengths (Surace et al., 1998; Tadhunter et al., 2005), which may have been formed as a consequence of the merger. Moreover, evidence for prodigious hidden star formation activity is provided by the detection of a large far-IR excess by the *IRAS* satellite ( $L_{IR} = 1.7 \times 10^{12} M_{\odot}$ , (Evans et al. 1999)). In addition, the CO observations indicate the presence of a substantial reservoir ( $3.3 \times 10^{10} M_{\odot}$ ) of molecular gas within  $\sim 2.5$  kpc of the active (western) nucleus ( $\rho > 2000 M_{\odot} \text{ pc}^{-3}$ : Evans et al. 1999), consistent with measurements in other ultraluminous infrared galaxies (Bryant & Scoville, 1999). The double nucleus, the distorted large-scale morphology, the presence of a rich inter-stellar medium (ISM) and YSPs clearly indicate that PKS1345+12 represents the later stages of a merger involving at least one gas-rich galaxy (Heckman et al., 1986; Surace et al., 1998).

For the imaging part of the project we have used HST archive data taken with various cameras and filters sensitive from the UV to the near-IR. The wide spectral coverage of the observations allows us to make accurate estimates of the ages of the stellar population associated with the bright knots identified in the images. For the spectroscopy we have used high-quality long-slit spectra presented in Holt et al. (2003). The spectroscopic data enable us to investigate the ages and mass contributions of the YSP detected at optical wavelengths in the diffuse halo of the galaxy. We compare the results with model predictions in order to understand the past and future of PKS1345+12.

## 2 OBSERVATIONS AND DATA REDUCTION

### 2.1 HST DATA

The HST dataset comprises four sets of images taken with the FOC, WFPC2, ACS and NICMOS cameras. A summary of the observations is presented in Table 1.

The observations and data reduction of the FOC images are described in Hurt et al. (1999). These pre-costar images were taken with the f/96 relay, with a combination of the F320W filter and three different polarizing filters (POL0, POL60 and POL120). The central wavelength of this configuration is  $\lambda_c = 3100 \text{ \AA}$  for a power-law spectrum  $f_{\lambda} \propto \lambda^{-1}$ .

For the purpose of this paper we are not interested in the polarization, but rather the total flux at various wavelengths. Therefore we adapted the data to make them suitable for

Camera	Filter	$\lambda_c(\text{\AA})(\text{rest frame})$	$\Delta\lambda(\text{\AA})(\text{rest frame})$	Exposure Time(sec)
FOC	F320W-POL0	2766	752	602
FOC	F320W-POL60	2773	752	529
FOC	F320W-POL120	2766	752	602
WFPC2	F439W	3844	423	2200
WFPC2	F814W	7127	1567	835
ACS(HRC)	FR459M	4539	410	2480
ACS(HRC)	F550M	4973	488	2480
ACS(WFC)	FR647M	5897	530	800
ACS(WFC)	FR647M	6549	588	800
NICMOS	F110W	10060	5349	95
NICMOS	F160W	14316	3566	95

**Table 1.** Summary of the HST observations of PKS1345+12 used in this paper

knot number	F320W	F439W	FR459M	flux(/ $10^{-18}$ erg sec $^{-1}$ cm $^{-2}$ $\text{\AA}^{-1}$ )					F110W	F160W
				F550M <sup>b</sup>	FR647M	F647M <sup>b</sup>	F814W			
C1	2.86 $\pm$ 0.57	2.09 $\pm$ 0.15	1.55 $\pm$ 0.06	1.35 $\pm$ 0.05	0.75 $\pm$ 0.05	1.30 $\pm$ 0.05	0.70 $\pm$ 0.05	<0.40	<0.24	
C2	1.44 $\pm$ 0.29	1.68 $\pm$ 0.12	1.35 $\pm$ 0.05	1.11 $\pm$ 0.04	0.98 $\pm$ 0.05	1.43 $\pm$ 0.06	0.69 $\pm$ 0.05	<0.40	<0.24	
C3 <sup>a</sup>	...	...	...	...	0.88 $\pm$ 0.05	1.35 $\pm$ 0.05	0.45 $\pm$ 0.04	...	...	
C4	1.56 $\pm$ 0.30	1.17 $\pm$ 0.10	0.71 $\pm$ 0.03	0.76 $\pm$ 0.03	0.58 $\pm$ 0.04	0.96 $\pm$ 0.04	0.35 $\pm$ 0.04	<0.40	<0.20	

**Table 2.** Fluxes measured for the clusters at various wavelengths from the HST images.

<sup>a</sup>For C3 we were only able to obtain accurate photometry for three photometric bands, due to the proximity of this cluster to one of the nuclei (see Fig 1).

<sup>b</sup>These two filters contain the [O III] and H $\alpha$  emission lines.

this study. Since the three images were taken at the same wavelength, we averaged them using the IRAF routine IMCOMBINE. Assuming that the light from the bright knots is unpolarized—a reasonable assumption—the polarizing filters will transmit half of the total flux. Therefore the fluxes derived from these data using the standard photometric calibration factors were multiplied by a factor of two in order to work out the total fluxes. The absolute photometric accuracy of the f/96 relay is 10 – 20 % Baum (1994).

The WFPC2 observations and their reduction are described in detail by Surace et al. (1998). The PKS1345+12 images were centred in the PC chip (0.046 arcseconds pixel $^{-1}$ ). The filters used were F439W and F814W, which are very similar to the standard Johnson B and Cousins I filters (Holtzman & et al., 1995a,b). Dark subtraction, bias subtraction and flat fielding were carried out using the standard data reduction pipeline procedures at STScI. The images were combined using the IRAF/STSDAS routine CRREJ which removes cosmic rays in the combined image. The calculated errors on the photometric points, including both the photon noise and calibration uncertainty, are  $\pm$ 7-10 per cent.

Four ACS images of PKS1345+12 are used in this paper. The Wide Field Channel (WFC: 0.049 arcseconds pixel $^{-1}$ ) was used in combination with FR647M medium band ramp filter to take two of the images, one centred on the redshifted H $\alpha$  emission line wavelength (hereafter H $\alpha$  image), and the other centred on the nearby continuum (hereafter H $\alpha$  continuum image).

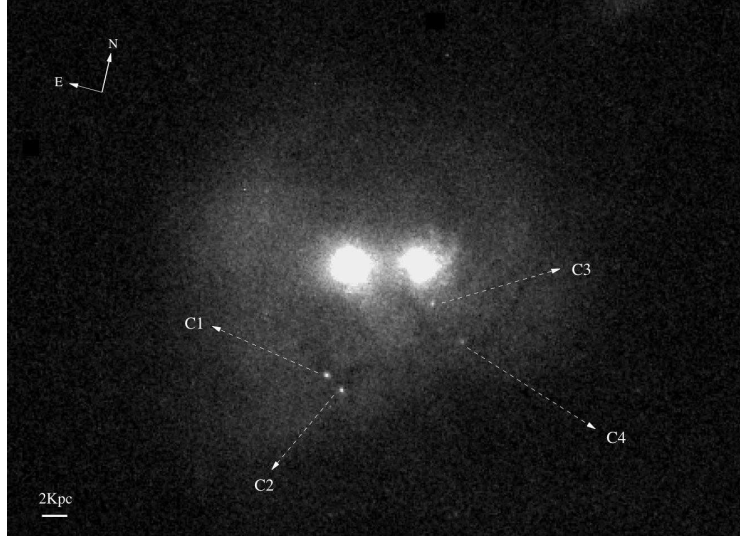


**Figure 1.** The ACS  $H\alpha$  continuum image of PKS1345+12 showing the presence of two nuclei, a distorted halo and four bright compact clusters embedded in this halo. The image also shows the presence of dust features spread to the south of the galaxy. These dust features intercept the positions of three of the clusters (C1,C2,C4).

The High Resolution Channel (HRC: 0.027 arcseconds pixel<sup>-1</sup>) was used in combination with F550M medium band filter ( $\lambda_0 = 5579 \text{ \AA}$   $\Delta\lambda_{FWHM} = 547 \text{ \AA}$ ) and FR459M medium band ramp filter to take the other images. In the former, the aim was to take an image of the galaxy at the wavelength of the [O III] $\lambda 5007$  emission line (hereafter O III image), whereas in the other images the pivot wavelength was chosen to take an image of the continuum near the [O III] $\lambda 5007$  line (hereafter O III continuum image). The FR647M( $\lambda_c = 6615 \text{ \AA}$ ) image is shown in Figure 1. The data were reduced following the standard data reduction pipeline procedures at STScI which employ two packages: CALACS package, which performs dark subtraction, bias subtraction and flat field corrections producing calibrated images, and MULTIDRIZZLE package which corrects for distortion and performs cosmic rays rejections. Since two of the ACS images were set up to measure the  $H\alpha$  and [O III] $\lambda 5007$  emission lines, they were not suitable to be used for modelling the continuum, and only the FR647M ( $\lambda_0 = 6615 \text{ \AA}$ ) and FR459M images were used for that purpose. The calculated errors of the photometric points including both the photon noise and calibration uncertainty are  $\pm 5\text{-}7$  per cent.

For the FOC, WFPC2 and ACS data, the routine PHOT in IRAF was used to measure sky-subtracted fluxes for the clusters within circular apertures typically 3-10 pixels in radius,

correcting for aperture losses using a synthetic PSFs generated with the TINYTIM program. The measured fluxes are summarised in Table 2.

The observations and reduction of the NICMOS data are described in Scoville et al. (2000). The images were taken using camera 2 of NICMOS, having a spatial resolution of 0.0762 and 0.0755 arcseconds pixel<sup>-1</sup> in x and y respectively (Thompson et al., 1998). The F110W(1.10  $\mu$ m,  $\Delta\lambda_{FWHM} \sim 0.6 \mu$ m), F160W(1.60  $\mu$ m,  $\Delta\lambda_{FWHM} \sim 0.4 \mu$ m) filters were used for the observations. The images we used for this paper were fully reduced and calibrated using the standard pipeline procedure.

No SSCs are clearly visible in the NICMOS images. However, the images are useful for measuring upper limits, which provide constraints on the long wavelength SEDs. For that purpose, the TINYTIM program was used to create synthetic point source images for each filter which were scaled using a range of flux scaling factors. The synthetic point sources were then added to the images at the expected locations of the SSC, and the flux scale factor increased until the point sources were just detected in visual inspection of the images. The fluxes of the just-detected point sources were taken as upper limits on the true near-IR fluxes of the SSC. We summarize the results based on the NICMOS data in Table 2.

## 2.2 Spectra

In addition, we have used long-slit spectra to study the YSP associated with the diffuse light component in PKS1345+12. The observations and reduction processes are described in Holt et al. (2003). The spectra were taken in 2001 May with the ISIS spectrograph on the 4.2m William Herschel Telescope (WHT) on La Palma. The final wavelength range is 3275-6813  $\text{\AA}$  in the blue and 6212-7720  $\text{\AA}$  in the red. Useful spectra were taken along two slit positions: PA 160 and PA 230 with a 1.3 arcsecond slit. The final wavelength calibration accuracy was 0.059  $\text{\AA}$  and 0.112  $\text{\AA}$  in the red and blue respectively, the spectral resolution is  $3.66 \pm 0.09 \text{\AA}$  in the red and  $4.54 \pm 0.10 \text{\AA}$  in the blue, and the relative flux calibration accuracy is  $\pm 5$  per cent. A preliminary analysis of this dataset for one aperture is presented in Tadhunter et al. (2005), whereas for the current study several apertures were extracted and analysed from both slit positions using the STARLINK packages FIGARO and DIPSO. Prior to modelling, the spectra were corrected for galactic reddening ( $E(B - V) = 0.034$ : Schlegel et al. (1998)) and we also subtracted the nebular continuum for those apertures with strong emission lines (Dickson et al., 1995; Holt et al., 2003). In the case

of the nuclear aperture, where we have a good estimate of the reddening of the various kinematic components, the optimum reddening model of Holt et al. (2003) was used to generate a nebular continuum. However, for apertures 1 and 2 the reddening is not known accurately because of the effect of the underlying absorption lines on the high order Balmer lines. For those apertures we used H $\alpha$  to generate the nebular continuum and considered two extreme cases: (i) maximum nebular continuum assuming no reddening of the emission line region; (ii) zero nebular continuum corresponding to high reddening. In the remaining apertures (PA 230, A & B; PA 160, 3 & 4) no nebular continuum subtraction was deemed necessary. We then performed spectral synthesis modelling of all the extracted spectra; the results are presented in next section.

### 3 RESULTS

#### 3.1 Photometric Analysis

The deep ACS H $\alpha$  continuum image presented in Figure 1 shows the presence of the two nuclei of this double nucleus system, as well as a common non-elliptical, distorted, halo of diffuse light surrounding the galaxy. Four bright super star clusters (SSC)<sup>3</sup> are clearly identified in the image and are the subject of our photometric analysis. Dust lanes are also detected as fine, extended features of lower surface brightness in the extended halo to the south of the galaxy. Significantly, the most prominent of these dust lanes intercept the positions of three of the SSC (C1, C2, C4). We further note that one of the clusters (C3) is close to the western nucleus. Due to this proximity, the flux measurements are less reliable for this cluster because of the large gradient in the galaxy background light. Moreover, for some of the images this cluster is not clearly detected. Therefore, it has not been considered in the modelling process.

Rather than the colour-colour or colour-magnitude diagrams that have been used previously to determine the ages of SSC in ULIRGs from multi-wavelength HST imaging observations (Surace et al., 1998; Wilson et al., 2006), we instead adopt the approach of modelling the optical/UV spectral energy distributions (SEDs) derived from our photometric measurements. The main advantage of this approach is that it utilises all of the photometric information simultaneously, and thereby allows both the reddening and age of each cluster

<sup>3</sup> Although these bright knots appear unresolved, at the distance of PKS1345+12 we cannot rule out the idea that they represent multiple star cluster systems rather than single SSC.

to be determined, without the age/reddening degeneracy that can be a problem for single colour-colour and colour-magnitude diagrams.

Stellar population synthesis models in the GALAXEV (version 2003) library (Bruzual & Charlot, 2003) were used to estimate the ages and masses of clusters C1, C2 and C4 from their respective SEDs. We used the *galaxevpl* program within the library to construct synthetic SSC spectra with ages in the range 1Myr to 11Myr. These spectra were created assuming an instantaneous burst of star formation, solar metallicity and using the Salpeter (1955) IMF with lower and upper mass cutoffs  $m_L = 0.1 \text{ M}_\odot$  and  $m_U = 100 \text{ M}_\odot$ . Reddened model spectra were created for the reddening range  $0.0 < E(B - V) < 1.0$  using the parametrized Galactic extinction law of Seaton (1979). The five photometric UV/optical points suitable for the fit, i.e. those not affected by emission line contamination, were modelled using a minimum  $\chi^2$  technique to find the ages of the SSC. Table 3 presents ranges of ages and reddenings for which acceptable fits were obtained ( $\chi^2_{red} \lesssim 1$ ); the ranges of measured masses are also presented. During the fitting process, the same ( $\pm 10\%$ ) error was assumed for all five photometric points. Taking in account the calibration error and the photon noise, both already discussed in section 2.1, plus small shifts in the central wavelengths of the filters, and uncertainties due to the gradient in the background near the clusters, we believe that a mean error of  $\pm 10\%$  is realistic.

The best fitting models for the three clusters are shown in Figure 2. For comparison, some models that fall outside of the range of acceptable fits are also shown. The latter represent the models with age/reddening combinations that give the best reduced chi-squared just outside the acceptable zone. Taking the example of cluster C2 (see Figure 2b) the fit obtained for the 4 Myr with  $E(B-V)=0.5$  model is noticeably better than that obtained for either the 3 Myr with  $E(B-V)=0.6$  or 6 Myr with  $E(B-V)=0.4$  models. Moreover  $\chi^2_{red}$  values found for YSP ages of 4-5 Myr and reddening of  $E(B-V)=0.5$  are  $\lesssim 1$ , while those found outside this range of ages are  $\gtrsim 2$ . Therefore, the range of ages considered to be valid for the case of C2 is 4-5 Myr, with the best fit found for a template of 4 Myr with a reddening of  $E(B-V)=0.5$ . Note that the high fluxes observed for the FOC F320W point for the three clusters, rule out starburst ages above 50 Myr, even taking in account any reddening effect, since the observed  $U - B$  is already bluer than such a starburst.

Further evidence for the young ages measured for the SSC in PKS1345+12 is provided by the detection of emission lines from the clusters in both the HST images (Figure 2) and the spectra (see next section). Based on the fluxes determined from our  $\text{H}\alpha$  emission line images,

**Table 3.** The results of the spectral synthesis modelling applied to the optical/UV photometric points of Table 2.

knot number	Age(Myr)	E(B-V)	Mass( $10^6 M_\odot$ )
C1	<7	0.2-0.5	$\sim 2.5 - 9.0$
C2	4-5	0.5	$\sim 4.0 - 4.8$
C4	<7	0.2-0.5	$\sim 1.3 - 5.0$

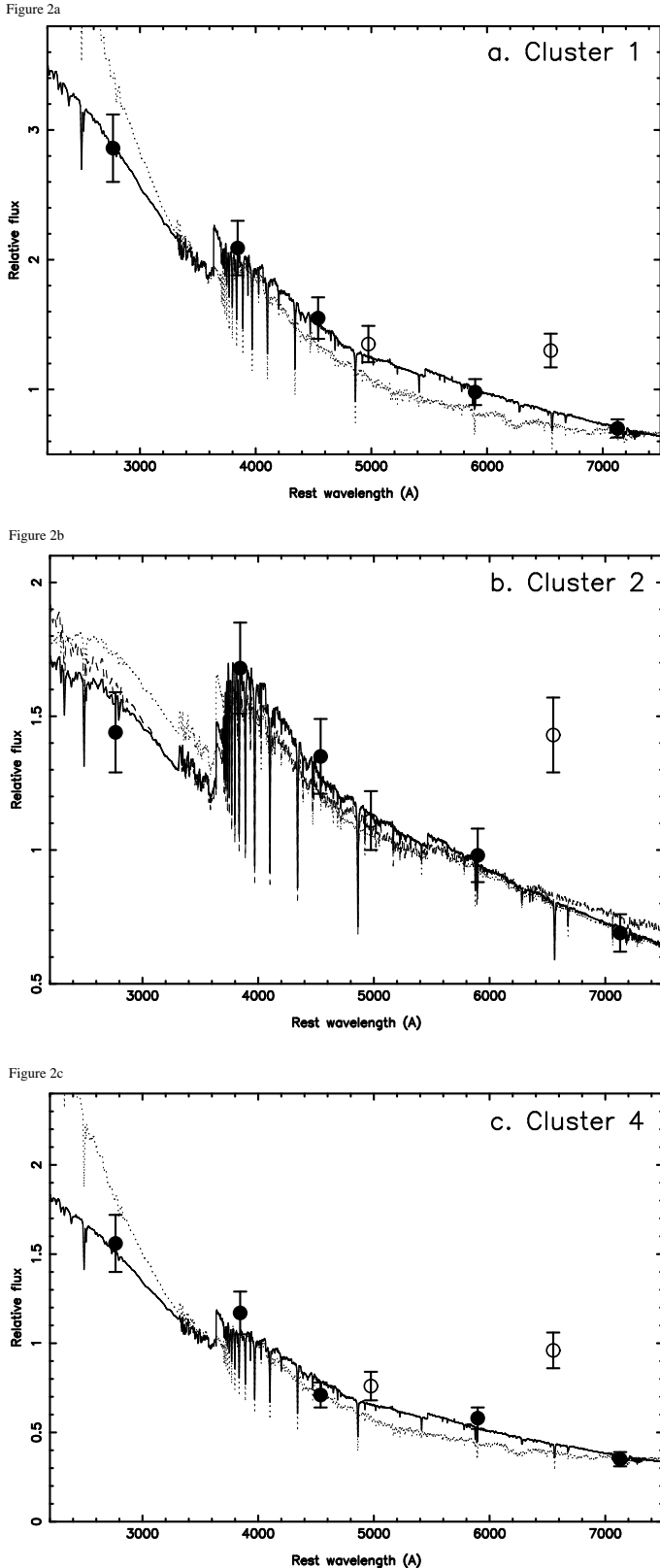
and correcting for both the SSC continuum and a 40% contribution from [NII] $\lambda\lambda 6548,6584$  emission lines in the filter bandpass, we determine H $\alpha$  equivalent widths of  $250 \pm 37$ ,  $370 \pm 34$  and  $606 \pm 86$  Å for clusters C1, C2 and C4 respectively. The instantaneous burst models of Leitherer et al. (1999) show that such high equivalent widths are only attained for clusters with ages  $t_{cl} < 6$  Myr, regardless of the assumed IMF. Since the ISM in the clusters may not absorb all the ionizing photons generated by the OB stars (as assumed by the Leitherer et al. 1999 models), the ages could be significantly less than this upper limit. Thus the detection of H $\alpha$  emission lines with high equivalent width is consistent with the range of ages determined from SED modelling of the clusters<sup>4</sup>. Finally we note that the NICMOS upper limits rule out ages older than  $\sim 11$  Myr with reddenings similar to or lower than those presented in Table 3, or ages  $< 7$  Myr with higher reddening values than the models in Table 3.

The masses of the SSC detected in PKS1345+12 ( $10^6 < M_{ssc} < 10^7 M_\odot$ ) are comparable with those of the most massive clusters detected in the Milky Way (e.g. Omega Centauri), in merger systems such as the ULIRG Arp220 (Wilson et al., 2006) and The Antennae (Fall et al., 2005), and in some other interacting systems (de Grijs et al., 2003). Given the difficulty of detecting individual SSC at the relatively high redshift of PKS1345+12, it is not surprising that the clusters we have detected are relatively young and massive. Certainly, our imaging observations do not rule out the presence of a more numerous cluster population in the halo of PKS1345+12, comprising SSC that are older and/or less massive than C1, C2 and C4.

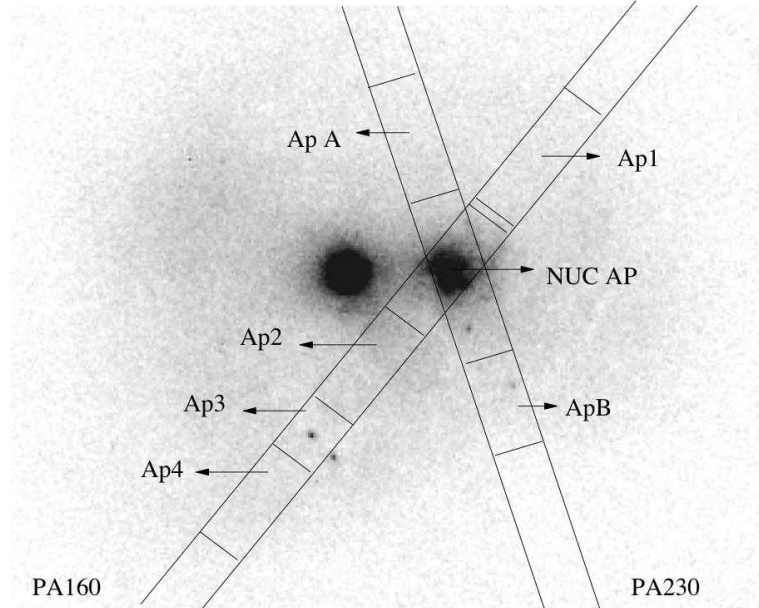
### 3.2 Analysis of the Spectra

Figure 3 shows the slit positions and the apertures used for the spectroscopic analysis. The same routine as described above was used to create simple stellar population templates of different age and reddening. Reddened model spectra were created using E(B-V) values

<sup>4</sup> Note that, although we have not been able to make detailed fits to the continuum SED of cluster C3, it is clear from Table 1 that this cluster also has H $\alpha$  detected at high equivalent width, and therefore it is also relatively young ( $t_{cl} < 6$  Myr).



**Figure 2.** The results of fitting different templates to the fluxes measured for the three clusters used in the photometric analysis (flux measurements shown by solid symbols). Figure 2a shows the fits obtained for C1 using templates of 2 Myr with  $E(B - V) = 0.5$  (solid line) and 8 Myr with  $E(B - V) = 0.1$  (dotted line). It is clear in the figure that a better fit is obtained for the template of 2 Myr. Figure 2b shows the plots obtained after fitting a 3 Myr template with  $E(B - V) = 0.6$  (dotted line), 4 Myr with  $E(B - V) = 0.5$  (solid line), and 6 Myr with  $E(B - V) = 0.4$  (dashed line) to the data of C2. In this case it is clear that the best fit is obtained for the 4 Myr template. Figure 2c shows the results of fitting templates of 2 Myr with  $E(B - V) = 0.5$  (solid line) and 8 Myr with  $E(B - V) = 0.1$  (dotted line) to the C4 data. The best fit this time is found for



**Figure 3.** H $\alpha$  continuum image showing the locations of the slits and the extraction apertures.

from 0.0 to 1.6 and the parametrized galactic extinction law of Seaton (1979). Each extracted spectrum was modelled using a combination of a young and an old stellar population (see Tadhunter et al. (2005)): we used a 12.5Gyr model for the old stellar population (OSP), adding YSP ranging in age from 0.001Gyr to 6Gyr (we will refer to this component as young component). For each spectroscopic aperture the continuum flux was measured in several wavelength bins ( $\sim 50$ ) chosen to be as evenly distributed in wavelength as possible, and to avoid strong emission lines and atmospheric absorption features. We then fitted these data using a minimum  $\chi^2$  technique to determine the best fitting age and reddening, as well as the relative contributions of each of the two populations. The result of the modelling the spectrum extracted for aperture Ap4 is shown in Figure 4 as an example.

Although the spectra have the advantage of considerably better wavelength sampling than the HST images, they have the disadvantage that several stellar populations of different age/reddening may be included in the large spectroscopic aperture. This can lead to an age-reddening degeneracy in the sense that adequate fits can sometimes be obtained for either a small proportion of a relatively young, highly reddened YSP plus an old stellar population, or a much larger proportion of an intermediate age, but less reddened YSP. Figure 5 presents the details of the minimum  $\chi^2_{red}$  modelling for aperture Ap1 and provides a good illustration this degeneracy problem (see also Tadhunter et al. 2005), since the two loci that represent adequate fits ( $\chi^2_{red} \lesssim 1$ ) are clearly separated in the figure: at around  $\sim 0.1$  Gyr with E(B-V)

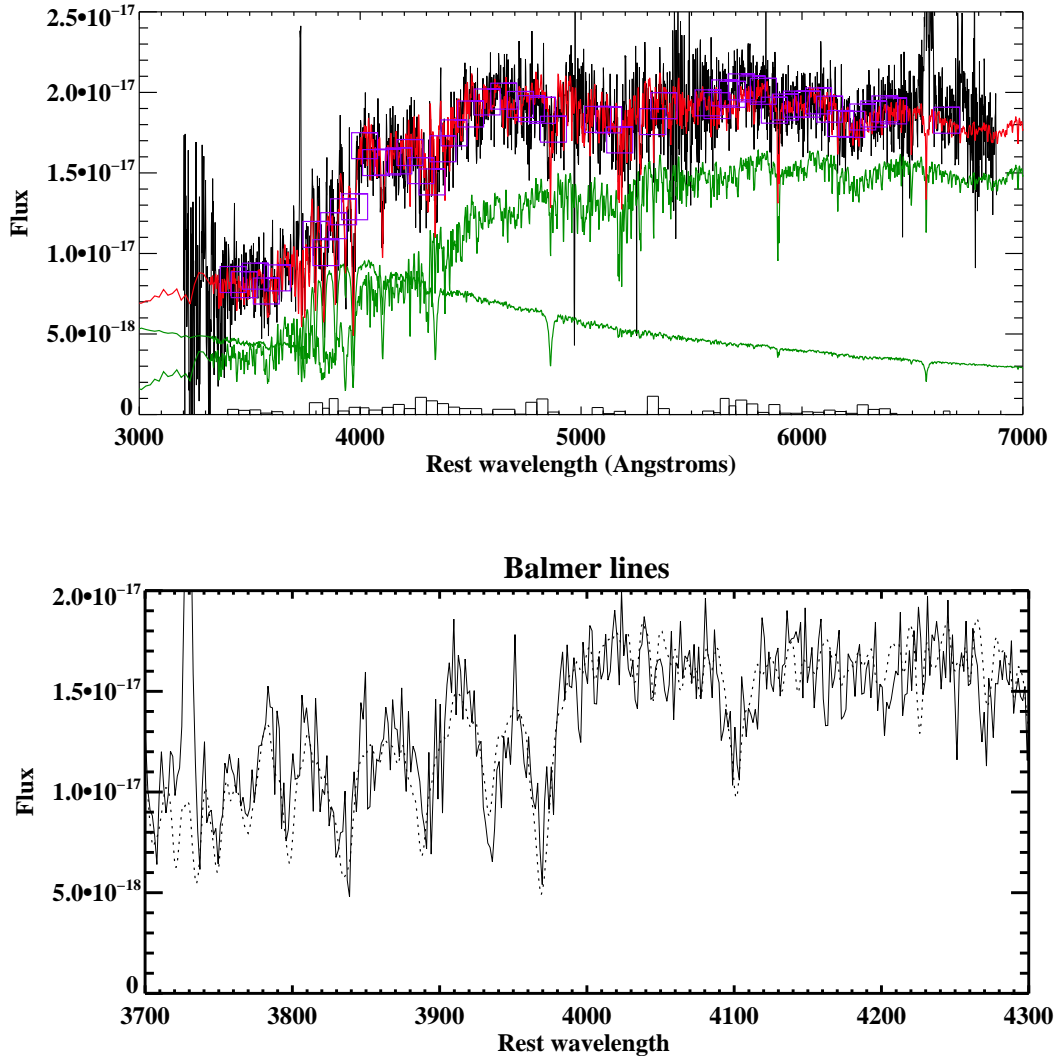


**Figure 4.** Upper panel: modelling result for the spectrum extracted from Ap4 of Fig 3. The green lines represent the young and old templates, while the red line represent their sum. The purple boxes represent the bins used for the fit, and the histogram on the x-axis represents the modulus of the error measured in each bin. In this case the young component has an age of 0.2 Gyr with a reddening of  $E(B-V) = 0.1$ . The contribution of this component to the total flux (red line) is 34.6 % in the normalising bin (4600-4700Å) and the  $\chi^2_{red}$  in this case is 0.4. Lower panel: detailed fit in the wavelength range 3700-4300. The fluxes are presented in wavelength units

$= 0.2$  and  $\sim 1.5$  Gyr with  $E(B-V) = 0.0$ . To distinguish between groups of templates that provide good fits, the model fits to the data were examined in detail, selecting those models which provide the best fit to the important absorption features of the spectra (for example CaII K, G-band, higher order Balmer lines). Figure 6 shows the wavelength range 3700Å — 4300Å for two of the best solutions obtained from the SED modelling of Ap3, PA160. It is clear from the plot, just by examining the features of the fit for the CaII H&K absorption lines, that in this case the model comprising 12.5 Gyr OSP plus the 0.04 Gyr YSP component age fits the data better than the 1.4 Gyr YSP model. However, there are cases (Ap2, Ap3, ApB)

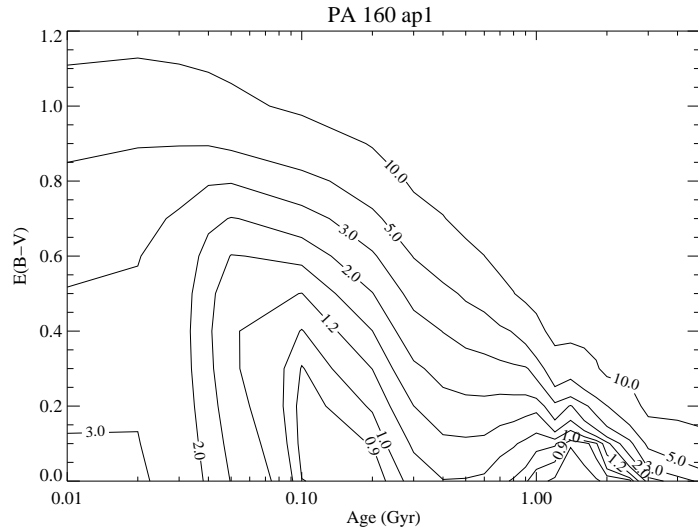


**Figure 5.** Minimum chi-squared fitting results for Ap1 in Figure 3. Each contour represents a value for  $\chi^2_{red}$ . Good results for the modelling are considered  $\chi^2_{red}$  of one or less (see discussion in Tadhunter et al. 2005). The two loci where good results are found are placed around 0.1 Gyr with  $E(B-V) = 0.2$  and 1.5 Gyr with no reddening

where even younger ( $\sim 0.005$  Gyr) age YSP — corresponding to the blue A/B supergiant phase — provide an adequate fit to the SED. For these latter cases we cannot distinguish between YSP with ages  $\sim 0.005$  Gyr and  $\sim 0.04$  Gyr using the detailed fits.

Table 4 summarizes the results of the modelling for all of the extracted spectroscopic apertures. We find ages for the YSP ranging from 0.005 Gyr to 1.5 Gyr with reddening in the range of  $E(B-V) = 0.0$  to 1.2. We also measured the mass contribution of the YSPs to the overall stellar mass in the aperture, finding results ranging from a negligible mass contribution ( $< 1\%$ ) in some apertures, to the YSP contributing a sizeable fraction of the total mass in others. The wide range of ages found for some of the apertures reflects the fact that good fits can also be achieved for two combinations of age/reddening (the degeneracy problem discussed above), and also depends on the nebular continuum subtraction (for Ap1 and Ap2). The reader may notice that the results for NUC AP in Figure 3 are not presented in Table 4. After the nebular subtraction, the flux contribution of the YSP in the normalising bin is small ( $< 10\%$ ). Therefore we find good fits for the entire range of combinations OSP and YSP templates.

It is notable that for the region to the south of the nucleus that encompasses the SSC detected in the HST images (i.e. Ap2, Ap3 and ApB), the minimum age that provides an adequate fit to the SED of the diffuse light ( $\sim 0.005$  Gyr) is consistent with the ages of the SSC measured in our photometric study, although older YSP ages ( $> 0.04$  Gyr) are also acceptable. On the other hand, we can *only* obtain adequate fits to the SEDs of the

		Age of YSP (Gyr)	E(B-V) <sup>a</sup>	%YSP of total mass
PA 160	Ap1	0.1 - 0.3	0.0 - 0.4	1.0 - 2.0
	Ap1-neb <sup>b</sup>	0.2 - 1.2	0.0 - 0.4	1 - 69
	Ap2	0.001 - 0.2	0.0 - 1.2	0.05 - 3.5
	Ap2-neb <sup>b</sup>	0.2 - 1.0	0.3 - 0.7	1 - 60
	Ap3	0.005 or 0.04 - 0.2	0.4 - 0.8 or 0.0 - 0.5	0.1 - 1.5 or 1.5 - 15.0
	Ap4	0.05 - 0.5	0.0 - 0.6	2 - 10
PA 230	ApA	0.05 - 1.5	0.0 - 0.4	2.0 - 90.0
	ApB	0.005 or 0.04 - 1.5	0.0 - 1.0 or 0.0 - 0.7	0.01- 1.2 or 7.0 - 90.0

**Table 4.** Results from the analysis of the spectra extracted from the apertures in Figure 3.

<sup>a</sup> The large range in reddening should be understood as it follows. For the younger solutions there is a wide range of reddening which gives good results. However, when moving towards older ages the amount of reddening needed for the template to match the data decreases as does the range.

<sup>b</sup> Two different sets of results are presented for the apertures 1 and 2. One is obtained from modelling without subtracting any nebular continuum from the spectra, while the other (labelled Ap1-neb and Ap2-neb) is obtained after having subtracted the maximum nebular continuum. Thus the true results are likely to fall between the the results presented in the table

other extended apertures (Ap1, ApA & Ap4) using older YSP with ages in the range 0.04 – 1.0 Gyr, and we cannot rule out the idea that YSP sampled by the diffuse light have the same age ( $\sim$ 0.1 – 0.3 Gyr) for all apertures.

Overall, the range of YSP ages we have determined for the diffuse light from our spectra of PKS1345+12 overlaps with the 1 – 300 Myr range determined for the YSP in the spectroscopic study of a sample of transitional ULIRG QSOs by Canalizo et al. (2001); it is also consistent with the 0.5 – 1.5 Gyr age determined by Tadhunter et al. (2005) for a single extended aperture to the SE of the nucleus of PKS1345+12 itself, although this latter study considered only unreddened YSP.

Finally we emphasise that the diffuse light contains the dominant YSP component in terms of mass. A lower limit on the total mass in the diffuse YSP component integrated across all our spectroscopic apertures is  $M_{diff}^{YSP} > 1.4 \times 10^9 M_{\odot}$ , and may be considerably larger if the regions of the galaxy not sampled by the slits are included. In contrast, the total mass in the three SSC with accurate age estimates is orders of magnitude less ( $8 \times 10^6 < M_{ssc}^{YSP} < 2 \times 10^7 M_{\odot}$ ).

### 3.3 Gas Kinematics in the Halo

The emission line kinematics of PKS1345+12 have been described in detail by Holt et al. (2003). As well as a quiescent emission line halo with relatively small radial velocity amplitudes ( $< 400 \text{ km s}^{-1}$ ) and linewidths ( $< 500 \text{ km s}^{-1}$  FWHM). Holt et al. (2003) found extreme kinematic components at the location of the western nucleus with velocity shifts up to  $\sim 2000 \text{ km s}^{-1}$  and line widths of  $\sim 2000 \text{ km s}^{-1}$  (FWHM) providing evidence for warm

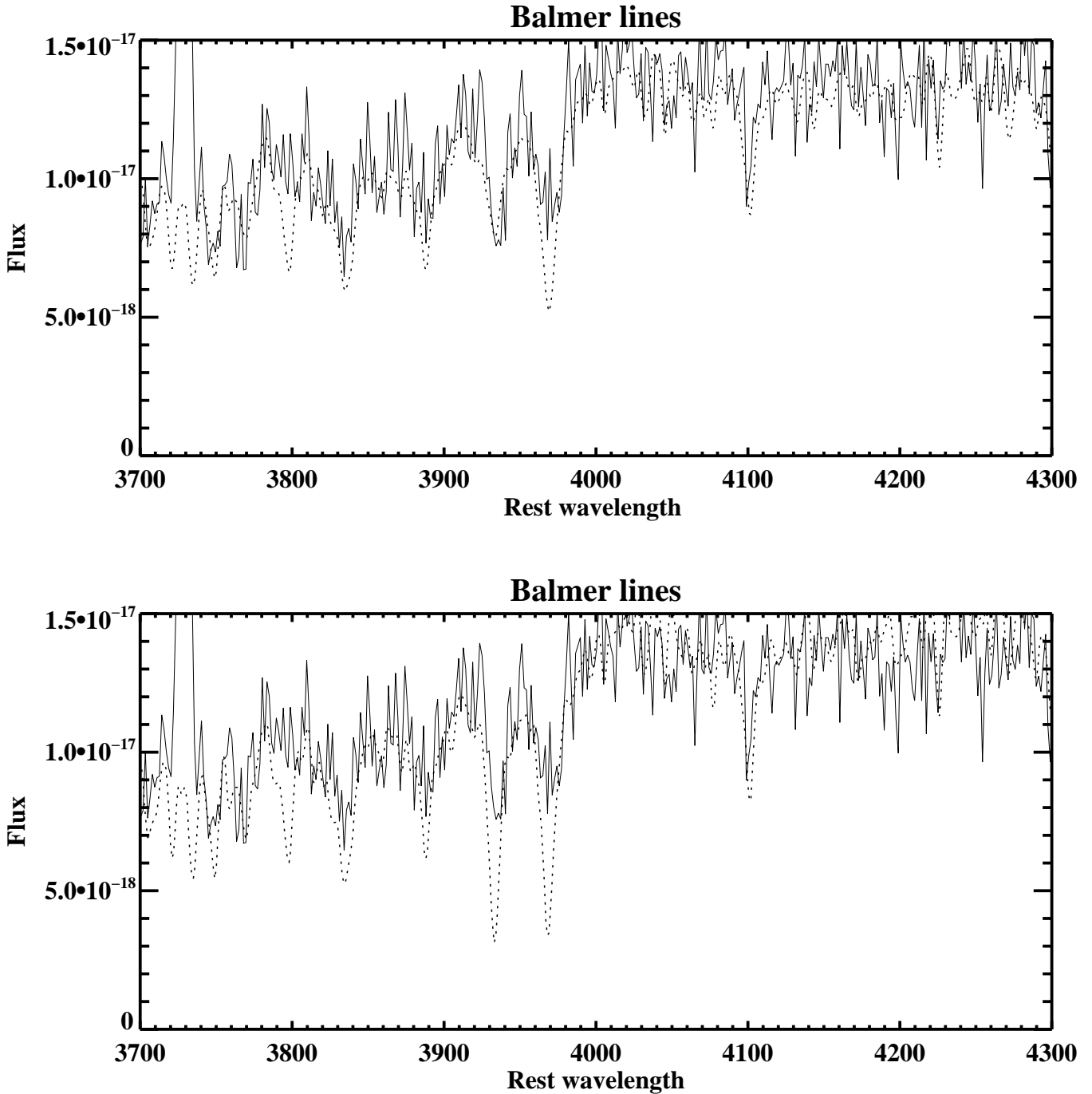


**Figure 6.** Detailed fits for the spectrum extracted from Ap3. Upper panel: detailed fit for a model with a young stellar component of 0.04 Gyr ( $E(B-V)=0.2$ ). Lower panel: detailed fit for a model with a “young” stellar component of 1.4 Gyr (no reddening). The fluxes are presented in wavelength units. It is clear from the figure that the model with the younger YSP (upper panel) fits the absorption features best, despite the fact that both models provide adequate fits to the overall SEDs.

gas outflows in the narrow line region. As mentioned in Section 3.1, we detect emission lines at the locations of the young star clusters visible in our HST in both the images and the long slit spectra. Therefore it is interesting to compare the kinematics of the star clusters with those of the other kinematic components in the galaxy.

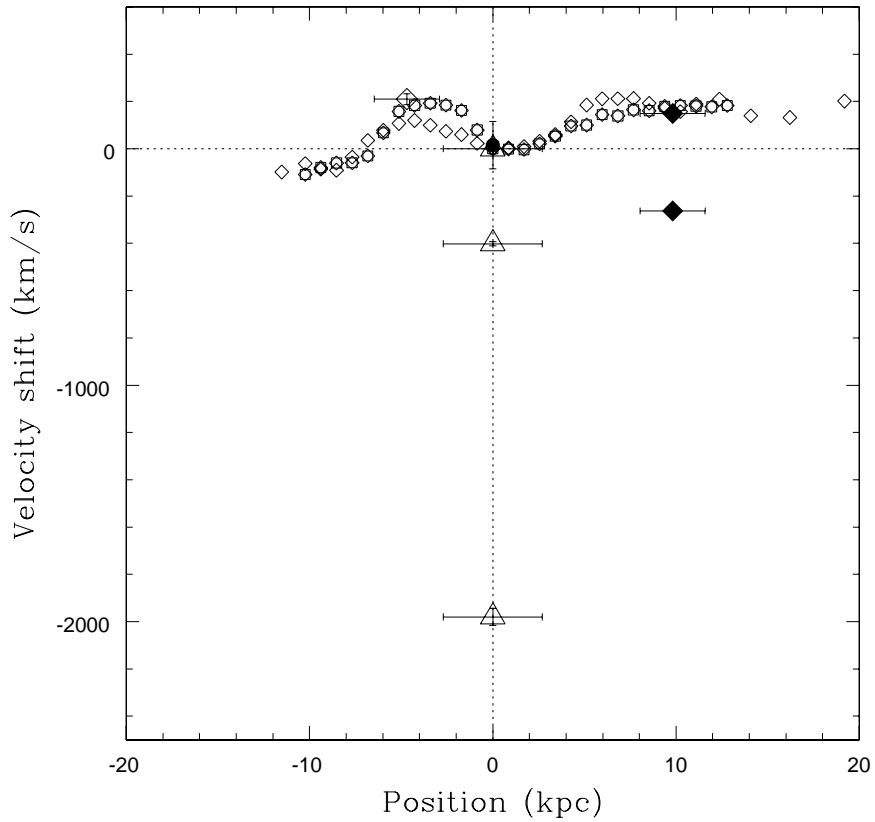


**Figure 7.** Spatial variations of the [O II] and H $\alpha$  radial velocities of the extended gaseous halo along PA 160. [O II] (open diamonds), H $\alpha$  (open diamonds + open squares). The error bars are small and are incorporated in the points. Overplotted is the radial velocity of the H I 21cm absorption (filled circle; Mirabel (1989)), the three components of [O III] in the nucleus (open triangles) and the extended emission line regions: the extended [O III] emission in the region to the NW (large open diamond) and the extended H $\alpha$  emission in the line splitting region to the SE coinciding with the position of the cluster C1 (large filled diamonds). Note: Positive kpc = south, negative kpc = north. The vertical dotted line represents the centroid of our nuclear aperture. The horizontal dotted line represents the velocity at the position of the centroid.

Figures 7 and 8 compare the emission line kinematics at the locations of the clusters with those of the spatially resolved diffuse gas detected in the H $\alpha$  and [OII] $\lambda 3727$  emission lines in the halo of the galaxy along PA 160 and PA 230. Intriguingly, we find clear evidence for line splitting in both H $\alpha$  and [OII] at the locations of clusters C1/C2 and C4. The line splitting is clearly visible in the extracted spectra of these regions shown in Figures 9 and 10 and also the grey scale representation of the long-slit spectra shown in Figure 11. Important features of the line splitting regions include the following.

- **Linewidths.** In both regions there is a relatively broad kinematic component ( $320 < FWHM < 400$  km s $^{-1}$ ) along with a narrower kinematic component ( $FWHM < 150$  km s $^{-1}$ ) that is spectrally unresolved.
- **Radial velocity shifts.** In both regions the broader component has a radial velocity

and line width consistent with that of the diffuse gas at larger and smaller radial distances from the nucleus, whereas the narrower component is significantly shifted relative to the diffuse gas: *blueshifted* by  $\sim 450$  km s $^{-1}$  for region C1/C2, and *redshifted* by  $\sim 300$  km s $^{-1}$  for region C4.

- **Ionization state.** Whereas the narrow kinematic component has relatively small [NII]6584/H $\alpha$  and [OIII]/H $\beta$  ratios ([NII]6584/H $\alpha$  < 0.5 and [OIII]/H $\beta$  < 1), consistent with photoionization by hot stars in an HII region (see Veilleux et al. 1999), the broader component has line ratios ([NII]6584/H $\alpha$  > 0.7 and [OIII]/H $\beta$  < 3) that are more consistent with LINER nuclei and the diffuse gas at other locations in the host galaxy. Overall the LINER-like line ratios for the broader diffuse gas component indicate ionization by shocks, or photoionization by an AGN at low ionization parameter.

All of these features are consistent with the idea that the narrow emission line components represent HII regions associated with the young star clusters, and that these SSC are moving at high velocity relative to both the ambient gas and the rest frame of the galaxy defined by the narrow emission lines and the HI 21cm absorption line detected in the nucleus. In this case, we are observing the clusters before the phase in which the supernovae associated with the massive stars in the clusters eject the ISM (Goodwin, 1997a,b; Bastian & Goodwin, 2006). Indeed, given that the supernova phase is expected to start  $\sim 3 - 4$  Myr after the birth of a star cluster (Leitherer et al. 1999), the ages we have determined for the SSC ( $\lesssim 6$  Myr) are consistent with such a supposition. Given their measured radial velocities and estimated ages, the clusters must have formed within a few kpc of their current locations, unless their tangential velocities are considerably larger than their radial velocities. This latter feature rules out the idea that the clusters formed at much larger radii in the outer halo of the merging system, then fell into the nuclear regions; *the gas out of which the SSC formed must have been moving rapidly prior to the formation of the star clusters.*

The alternative explanation, that we have caught the SSC in the ejection phase, and that the line splitting is caused by the ejection of gas by SSC formed in the quiescent, diffuse gas (Goodwin, 1997a,b; Bastian & Goodwin, 2006) is difficult to reconcile with the observations. In particular, in such a case it is not clear why the component apparently at rest relative to the ambient gas has relatively broad lines and a [NII]6584/H $\alpha$  ratio consistent with shocks or AGN photoionization, whereas the component shifted relative to the rest frame (presumably

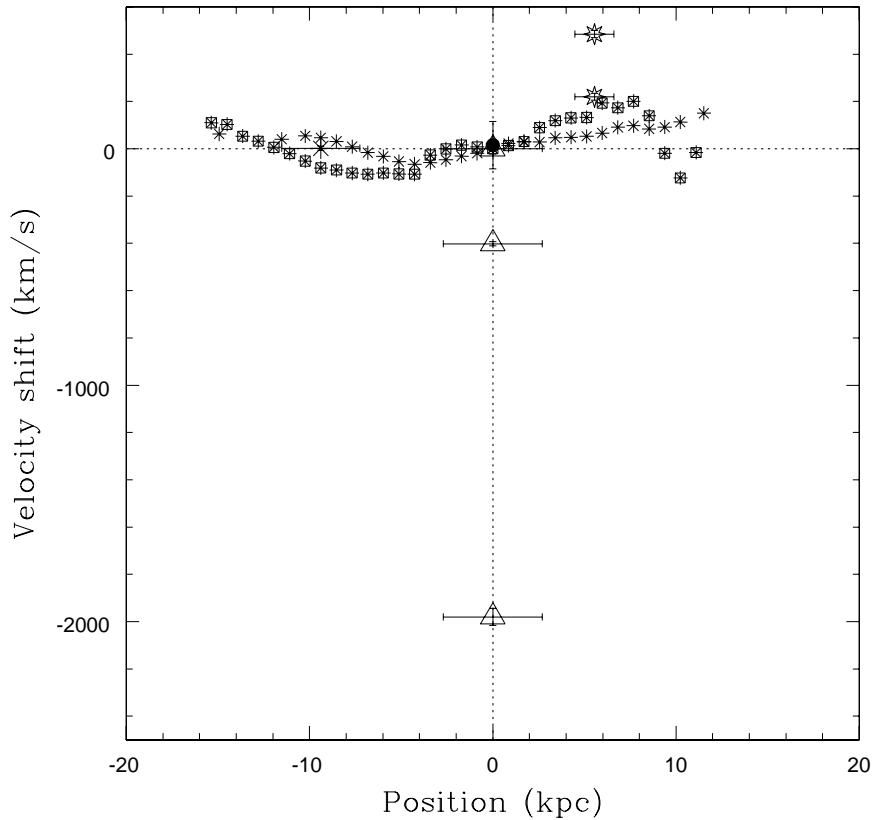


**Figure 8.** Same figure than 8 but for PA 230. [O II] (asterisks), H $\alpha$  (asterisks+ open squares). The error bars are small and are incorporated in the points. Overplotted is the radial velocity of the H $\text{I}$  21cm absorption (filled circle; Mirabel (1989)), the three components of [O III] in the nucleus (open triangles) and the extended emission line regions: the extended [O III] emission (large asterisk) and the extended H $\alpha$  emission in the line splitting region to the SW coinciding with the position of the cluster C4 (large stars). Note: Positive kpc = south-west, negative kpc = north-east. The vertical dotted line represents the centroid of our nuclear aperture. The horizontal dotted line represents the velocity at the position of the centroid.

the ejected component in this scenario) has narrow lines and an HII region-like [NII]/H $\alpha$  ratio characteristic of stellar photoionization; one would expect the reverse to be the case.

Finally we note that, despite the apparently “free-floating” status indicated by their emission line kinematics, the SSC/HII regions are linked with a more extensive interstellar medium (ISM) in the host galaxies. First, there is clear morphological evidence from our high resolution ACS images that the young star clusters are associated with dust lanes in the host galaxy (see Figure 1). Second, at the location of C1/C2, the greyscale representation of the long-slit spectrum (see Figure 11) shows a clear enhancement in the flux of *both* the broad and narrow components, suggesting a link between the HII regions and the more diffuse gas.

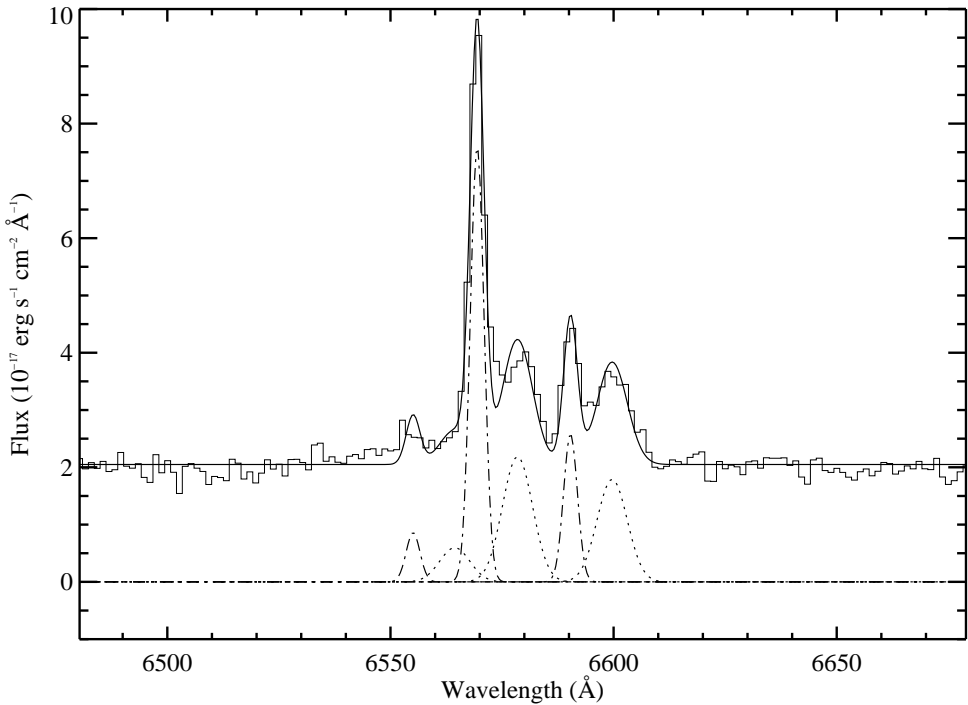


**Figure 9.** H $\alpha$  model of the region exhibiting line splitting coinciding with the position of C1. The faint line traces the observed spectra and the bold line represents the overall model profile. The six components, two for each line, are also overplotted — the dotted line traces the broader component consistent with the kinematics of the emission line gas at other locations in the galaxy, and the dot-dashed line traces the narrow component blueshifted by  $\sim 450$  km s $^{-1}$  with respect to the ambient gas.

## 4 DISCUSSION

### 4.1 Age determination for the YSPs in ULIRGs

It is interesting to compare our results for PKS1345+12 with previous studies of YSP in ULIRGs. Surace et al. (1998) carried out an HST imaging study concentrating on bright star forming knots for a sample of nine “warm” ULIRGs, including PKS1345+12, using high resolution B- and I-band images taken with the Wide Field Planetary Camera on the HST. The stellar synthesis models of Bruzual & Charlot (1993) were used to estimate the ages and masses of the bright knots in colour-magnitude diagrams. However, It is difficult to distinguish between stellar age and reddening using only B- and I-band observations. Thus the ages presented in Surace et al. (1998) are upper limits and, as discussed in that paper, the effect of correcting for the reddening could substantially modify the age and mass estimates, resulting in younger ages and smaller masses. For the whole sample, they derive a median upper limit for the age of  $\sim 3 \times 10^8$  yr and masses in the range  $10^5 < M_{clusters} < 10^9$  M $_{\odot}$ . In the case of PKS1345+12 itself, they found ages  $\sim 10^7 < t_{ssc} < 10^8$  yr and masses  $\sim 10^7 < M_{clusters} < 10^8$  M $_{\odot}$ . Since we have measured significant amounts of reddening

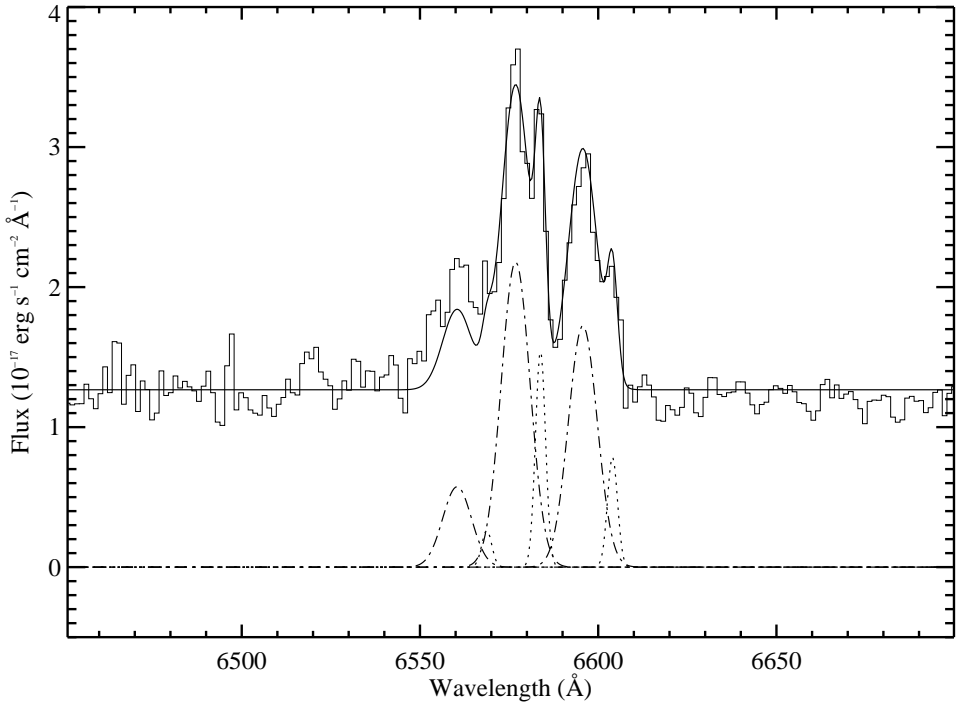


**Figure 10.** H $\alpha$  model of the region exhibiting line splitting coinciding with the position of C4. The faint line traces the observed spectra and the bold line represents the overall model profile. The six components, two for each line, are also overplotted — the dotted line traces the broader component, and the dot-dashed line trace the second narrow component redshifted by  $\sim 300$  km s $^{-1}$  with respect to the spatially extended narrow component

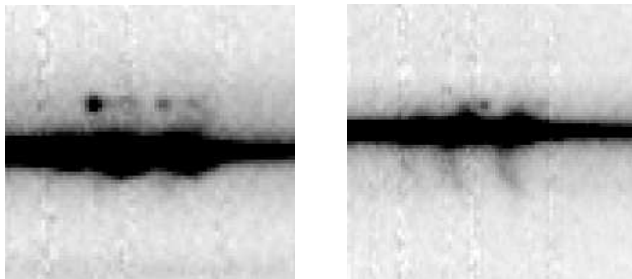


**Figure 11.** 2-D optical spectra for PA 160(left) and PA 230(right), centred on the redshifted H $\alpha$ +[NII] emission lines. The x axis is the wavelength direction increasing to the right, and the vertical axis is the spatial direction with SE to the top and NW to the bottom. The images show the regions exhibiting H $\alpha$  line splitting, coincident with the SSC, and demonstrate the flux enhancement of both kinematic in the line splitting region in PA 160 (at the location of C1/C2).

for the knots in PKS1345+12, this galaxy is clearly a case in which the reddening affects the results presented in Surace et al. (1998). As expected, after taking into account the reddening, we deduce younger ages and lower masses for the SSC in PKS1345+12.

It is well known that large amounts of gas and dust surround the AGN in the western nucleus of PKS1345+12 (Evans et al., 1999; Surace & Sanders, 1999; Scoville et al., 2000; Holt et al., 2003). Our new results demonstrate the importance of dust on a larger,  $\sim 5 - 15$  kpc scale, in the halo of the galaxy. Not only do the SED fits require a reddening in the

range  $0.2 < E(B - V) < 0.5$ , but there are dust structures in our images coincident with the SSC. Therefore it is dangerous to use single colour-magnitude diagrams to determine the ages of the YSPs in such objects.

As well as the importance of taking into account reddening, our results also demonstrate that imaging and spectroscopic data provide complementary information about the YSPs; clearly a combination of the two types of data is required to make a full census of the YSPs present in systems of this type. Whereas on the basis of photometric analysis we find robust ages  $< 6$  Myr for the three SSC with good SEDs, our spectroscopic analysis places a lower limit of 40Myr on the ages of the YSP associated with the diffuse light in three of the regions sampled by our spectra. Therefore, our results demonstrate that the highest surface brightness regions (in this case the SSC) can give a misleading impression of the properties of the YSP component associated with the diffuse light in the galaxy as a whole.

## 4.2 The past and future of star formation in PKS1345+12

Combining both imaging and spectroscopic techniques, we find evidence for two distinct phases of recent star formation activity in PKS1345+12: one occurring less than 6 Myr ago that is associated with the SSCs and perhaps also linked to current the AGN and ULIRG activity; the other occurring more than 40 Myr ago and associated with the diffuse light. This is consistent with previous HST imaging studies which have shown evidence for more than one episode of star formation activity in other merging systems including the Antennae (Whitmore et al., 1999), NGC7252 (Miller et al., 1997; Maraston et al., 2001), and Arp220 (Wilson et al., 2006). Therefore our results fit in with the emerging trend that the star formation in merging systems is complex and multi-modal.

At this stage it is important to add the caveat that, although we have assumed that all of the YSP in PKS1345+12 formed in starbursts triggered by the merger, an alternative explanation is that the older YSP component associated with the diffuse light represents the captured disk of one of the merging galaxies i.e. the diffuse light YSP is not directly associated with the merging process. To test this latter scenario we have attempted to model the spectra of the diffuse light for all apertures using template spectra for disk galaxies of Sa and Sb morphological types taken from Kinney et al. (1996). We find good fits with either Sa or Sb templates for Ap 1, Ap2, and Ap A and Ap B. Although no good fits are found ( $\chi^2_{red} > 2$ ) for the other apertures, the Kinney et al. (1996) templates represent averages for

several galaxies of the same morphological type, and each galaxy type template encompasses a range of individual galaxy spectra, some of which deviate substantially from the average SED. Therefore we cannot absolutely rule out the idea that the YSP detected in the diffuse light for these apertures are associated with the disrupted disk(s) of one or more of the merging galaxies. Overall it is entirely plausible that the YSP associated with the diffuse light represent the captured stellar population from one or more merging disk galaxies, rather than stars formed in the merger itself

Are our results consistent with the numerical simulations of major galaxy mergers? For the case of a merger between two galaxies with substantial bulges — the likely scenario for PKS1345+12 — the simulations predict that the major merger-induced starburst occurs as the two nuclei finally merge together, but that there will also be a lower level of interaction-induced star formation activity at an earlier stage due to the tidal effects of the interaction on the disks of the individual merging galaxies (Barnes & Hernquist, 1996; Mihos & Hernquist, 1996). Therefore it is plausible that the younger YSP represented by the SSC and the ULIRG activity are all related to the high gas densities produced in the final stages of the merger as the nuclei merge together. On the other hand, assuming that they are not captured disk populations, the older YSP associated with the diffuse light may represent the earlier phase of lower level interaction-induced star formation. In this case, the models predict that we should expect an even higher level of star formation and AGN activity over the  $\sim 10^7$  yr it will take for the nuclei to coalesce (Evans et al. (1999)).

### 4.3 Order of events in triggering the AGN

Several recent studies of YSP have been used to estimate the timescales and order of events for triggering the activity in radio galaxies. For their sample of three radio galaxies, Tadhunter et al. (2005) found relatively old post-starburst ages ( $\sim 0.3$  -  $2.5$  Gyr) compared with the lifetimes of the radio sources. Emonts et al. (2006) also found a significant ( $\sim 0.3$  Gyr) delay between the starburst event and Radio-AGN activity for the radio galaxy B2 0648+27. These results are consistent with a scenario in which the radio activity is triggered relatively late in the merger sequence, following the major merger-induced starburst. However, Tadhunter et al. (2005) also discussed the possibility that some radio sources have undergone multiple epochs of activity. Indeed, Stanghellini et al. (2005) detected low surface brightness extended radio emission surrounding several objects in their sample of oth-

erwise compact ( $D < 1$  kpc) radio sources, including PKS1345+12. Moreover, this galaxy shows some evidence for continuity between the compact and extended emission, which, if confirmed, would suggest that PKS1345+12 has had AGN-Radio activity over a longer timescale than the estimated age of the GPS source ( $<0.1$  Myr). Given the evidence for both multiple epochs of star formation, including some YSP with ages less than 6 Myr, and multiple epochs of radio jet activity, we conclude that there is no clear evidence for a delay between the merger-induced starburst and the start of the AGN phase in PKS1345+12.

#### 4.4 SSC kinematics

In Section 3.3 we presented evidence that the SSC and their associated HII regions are moving at high radial velocities relative to the diffuse ISM detected (in projection) at similar locations in the halo of the host galaxy, despite the morphological evidence for associations with diffuse ISM components. It is interesting to consider how such rapidly moving star clusters might form.

The first possibility recognises the fact that major galaxy mergers are violent events, and considerable dissipation must take place before the gas finally settles into a stable configuration in the merged system. At all stages in a merger, but particularly the final stages before the nuclei of the two merging galaxies coalesce, it is likely that rapidly moving gas streams/tidal tails will rain down on the central regions of the host galaxy. As individual gas streams collide with the ambient gas or other gas streams, they will generate shocks that may trigger star formation (Barnes, 2004). The ionizing photons generated in the shocks as the tidal streams interact with the ambient gas may also lead to a local enhancement in the emission line luminosity of the ambient gas, perhaps explaining the effect seen in Figure 11. Therefore the formation of the SSC detected in PKS1345+12 may be associated with the overall settling/dissipation process that must accompany the evolution of the ISM following a major galaxy merger; it is possible that we are witnessing the events that will eventually lead to the formation of a high velocity dispersion globular cluster systems (e.g. Ashman & Zepf (1992); Zepf & Ashman (1993)) as the host galaxy settles down to its final state as a quiescent elliptical galaxy.

A second possibility is suggested by the detection of diffuse radio emission extending  $\sim 35$  arcseconds ( $\sim 83$  kpc) to the north, and  $\sim 25$  arcseconds ( $\sim 60$  kpc) to the south, of the nucleus of PKS1345+12, and encompassing the region of the SSC (Stanghellini et al., 2005). As

discussed in the previous section, although the major, high surface brightness radio activity is now taking place on a sub-kpc scale close to the western nucleus (Stanghellini et al., 2005), the presence of diffuse radio emission on a much larger scale provides evidence that there was an earlier phase of activity in which the relativistic plasma jets escaped into the halo of the merging system. In this phase, the radially expanding jets and laterally expanding jet cocoon would have interacted strongly with the warm/cool ISM associated with the merger, shocking the gas and possibly triggering star formation (Rees, 1989; Begelman & Cioffi, 1989). Because the shocked gas is accelerated to high velocities by the jet-cloud interactions, it would be expected that any SSC formed in such interactions would be moving at a high velocity relative to the ambient ISM, as observed in PKS1345+12. Moreover, interaction with the expanding cocoon could produce both positive and negative radial velocities, depending on the interaction geometry. Therefore, the fact that C1/C2 is blueshifted, while C4 is redshifted, is not a problem for this model.

Note that the importance of jet-induced star formation as a mechanism remains controversial. The direct observational evidence for the mechanism remains sparse, confined to a few objects observed across a large range of redshifts (Best et al., 1997; Dey et al., 1997; Croft et al., 2006). There is also a recognition that hydrodynamic effects of the jet-cloud interactions, as well as the heating effects of the accompanying quasar activity, can be as destructive as they are conducive to star formation. However, the recent detection of high velocity neutral outflows against the cores of several compact radio sources (Morganti et al. 2005a, Morganti et al. 2005b) — including PKS1345+12 itself — demonstrates that, despite being accelerated to high velocities, the gas behind a shock can at least cool to a neutral phase. This lends weight to the plausibility of jet-induced star formation as a mechanism.

## 5 CONCLUSION

We have reported a detailed investigation of the YSP in the ULIRG PKS1345+12, combining information from both spectroscopic and imaging methods. Our key conclusions can be summarised as follows:

- **Reddening.** We find that the three SSC with good photometric information in our study are all significantly reddened. Clearly it is important to have sufficient photometric information with wide spectral coverage to remove any age-reddening degeneracy and determine accurate YSP properties, even for clusters in the extended halo of a galaxy.

- **High resolution imaging versus spectroscopy.** This study provides a clear demonstration of the fact that high resolution HST imaging studies tend to be biased towards the youngest and/or most massive individual star forming clusters, and may give a misleading impression of the star formation histories of the dominant YSP in terms of total mass (sampled by the diffuse light in PKS1345+12).
- **The star formation history of PKS1345+12.** We find evidence for a complex star formation history of the YSP in PKS1345+12, with at least two major phases of star formation, one of which may be associated with star formation in the merging disk galaxies at an earlier stage of the merger.
- **Order of events.** Unlike some other radio galaxies, we find no clear evidence in PKS1345+12 for a time delay between the major merger-induced starburst and the AGN activity.
- **Star cluster kinematics.** On the basis of our analysis of the emission line kinematics, we deduce that the SSC are moving at high velocity relative to ambient gas and the rest frame of the host galaxy. The extreme SSC kinematics may be related to the process of star formation as infalling gas settles in the nuclear regions in the final stages of the merger, or to star formation triggered by the expanding radio source as it drives shocks into the ISM.

## ACKNOWLEDGMENTS

We thank Enrique Perez and Simon Goodwin for useful discussions, and Katherine Inskip for technical IDL support. We also thank the anonymous referee for useful comments that have helped to improve the manuscript. JR and JH acknowledge financial support from PPARC. Based on observations with the NASA/ESA *Hubble Space Telescope*, which is operated by the Association for Research in Astronomy (AURA), Inc, under NASA contract NAS5-26555. The William Herschel Telescope is operated on the island of La Palma by the Isaac Newton Group in the Spanish Observatorio del Roque de los Muchachos of the Instituto de Astrofísica de Canarias.

## REFERENCES

- Ashman K., Zepf S., 1992, ApJ, 384, 50  
 Barnes J., 2004, MNRAS, 350, 798  
 Barnes J., Hernquist L., 1996, ApJ., 471, 115

- Bastian N., Goodwin S., 2006, MNRAS, in press, astro
- Baum S., 1994, Baltimore STScI, HST Data Handbook
- Begelman M., Cioffi D., 1989, ApJ, 345, L21
- Best P., Longair M., Rottgerring H., 1997, MNRAS, 286, 785
- Bruzual G., Charlot S., 1993, ApJ, 405, 538
- Bruzual G., Charlot S., 2003, MNRAS, 344, 1000
- Bryant P., Scoville N., 1999, Ap.J., 117, 2632
- Canalizo G., Stockton A., 2000a, AJ, 528, 201
- Canalizo G., Stockton A., 2000b, AJ, 120, 1750
- Canalizo G., Stockton A., 2001, ApJ, 555, 719
- Croft S., van Breugel W., Dopita M., Martin C., Morganti R., Neff S., Osterloo T., Schiminovich D., Stanford S., van Gorkom J., 2006, ApJ, 647, 1040
- de Grijs R., Anders P., Bastian N., Lynds R., Lamers H., O’Neil, Jr E., 2003, MNRAS, 343, 1285
- Dey A., van Breugel W., Vacca W., Antonucci R., 1997, ApJ, 490, 498
- di Matteo T., Springel V., Hernquist L., 2005, Nature, 433, 604
- Dickson R., Tadhunter C. N., Shaw M., Clark N., Morganti R., 1995, MNRAS, 273, L29
- Emonts B., Morganti R., Tadhunter C., Holt J., Oosterloo T., van der Hulst J., Wills K., 2006, A&A, 454, 125
- Evans A., Kim D., Mazzarella J., Scoville N., Sanders D., 1999, ApJ, 521, L107
- Fall S., Chandar R., Whitmore B., 2005, ApJ, 631, L133
- Goodwin S., 1997a, MNRAS, 284, 785
- Goodwin S., 1997b, MNRAS, 286, 669
- Heckman T., Smith E., Baum S., van Breugle W., Miley J., Illingworth D., Bothun G., Balick B., 1986, ApJS, 74, 833
- Holt J., Tadhunter C. N., Morganti R., 2003, MNRAS, 342, 227
- Holtzman J., et al. 1995a, PASP, 107, 156
- Holtzman J., et al. 1995b, PASP, 107, 1065
- Houck J., et al 1984, Ap.J., 278, L63
- Houck J., Sneider D., Danielson G., Beichman C., Lonsdale C., Neugebauer C., B.T. S., 1985, Ap.J., 290, L5
- Hurt T., Antonucci R., Cohen R., Kinney A., Krolik J., 1999, ApJ, 514, 579
- Kinney A., Calzetti D., Bohlin R., McQuade K., 1996, ApJ, 467, 38

- Le Floc'h E., Papovic C., Dole H., Bell E., Lagache G., Rieke G., Egami E., Pérez-González P., Alonso-Herrero A., Rieke M., Blaylock M., Engelbracht C., Gordon K., Hones D., Misselt K., Morrison J., J. M., 2005, *ApJ*, 632, 169
- Leitherer C., Schaerer D., Goldader J., Gonzalez Delgado R., Robert C., Foo Kune D., de Mello D., Devost D., Heckman T., 1999, *ApJ*, 123, 3
- Maraston C., Kissler-Patig M., Brodie J., Bramby P., Huchra J., 2001, *A&A*, 370, 116
- Mihos J., Hernquist L., 1996, *ApJ*, 464, 641
- Miller B., Whitmore B., Schweizer F., S.M. F., 1997, *AJ*, 114, 2381
- Mirabel I., 1989, *ApJ*, 340, L13
- Morganti R., Osterloo T.A. and Tadhunter C., van Moorsel G., Emants B., 2005, *A&A*, 439, 521
- Morganti R., Tadhunter C., Osterloo T., 2005, *A&A*, 444, L9
- Pérez-González P., Rieke G., Egami E., Alonso-Herrero A., Dolé H., Papovich C., Blaylock M., Jones J., Rieke M., Rigby J., Barmby P., Fazio G., Huang J., Matin C., 2005, *ApJ*, 630, 107
- Rees J., 1989, *MNRAS*, 239, P1
- Salpeter E., 1955, *ApJ*, 121, 161
- Sanders D. B., Mirabel I. F., 1996, *ARA&A*, 34, 749
- Sanders D. B., Soifer B. T., Elias J. H., Madore B. F., Matthews K., Neugebauer G., Scoville N. Z., 1988, *ApJ*, 325, 74
- Schlegel J., Finkbeiner D., Davis M., 1998, *ApJ*, 500, 525
- Scoville N. Z., Evans A. S., Thompson R., Rieke M., Hines D. C., Low F. J., Dinshaw N., Surace J. A., Armus L., 2000, *ApJ*, 119, 991
- Seaton M., 1979, *MNRAS*, 187, 73
- Soifer B., et al 1984a, *Ap.J.*, 278, L71
- Soifer B., et al 1984b, *Ap.J.*, 283, L1
- Stanghellini C., O'Dea C., Dallacasa D., Cassaro P., Baum S., Fanti R., Fanti C., 2005, *A&A*, 443, 891
- Surace J. A., et al 2000a, *ApJ*, 529, 170
- Surace J. A., et al 2000b, *ApJ*, 120, 604
- Surace J. A., Sanders D. B., Vacca W. D. Veilleux S., Mazzarella J. M., 1998, *ApJ*, 492, 116
- Surace J. A., Sanders D. C., 1999, *ApJ*, 512, 162

- Tadhunter C. N., Robinson T. G., Gonzalez Delgado R. M., Wills K., Morganti R., 2005, MNRAS, 356, 480
- Thompson R. I., Rieke M., Schneider G., Hines D. C., Corbin M. R., 1998, ApJ, 492, L95
- Whitmore B., Zhang Q., Leitherer C., Fall S., Schweizer F., Miller B., 1999, AJ, 118, 1551
- Wilson C., Harris W., Longden R., Scoville N., 2006, ApJ, 641, 763
- Zepf S., Ashman K., 1993, MNRAS, 264, 611